Advanced Materials

ADVANCED MATERIALS
www.advmat.de

RESEARCH ARTICLE

Ferroelectric-Configured In-Sensor Dynamic Computing with 2D Perovskites for Dim Object Recognition

Jie Liu[1] | Fan Du[1] | Limin Wu[1,2] | Xiaosheng Fang[1]

[1]College of Smart Materials and Future Energy and State Key Laboratory of Molecular Engineering of Polymers, Fudan University, Shanghai, P. R. China | [2]College of Chemistry and Chemical Engineering, Inner Mongolia University, Hohhot, P. R. China

Correspondence: Limin Wu (lmw@fudan.edu.cn) | Xiaosheng Fang (xshfang@fudan.edu.cn)

Received: 21 October 2025 | **Revised:** 12 December 2025 | **Accepted:** 16 December 2025

Keywords: bulk photovoltaic effect | ferroelectric materials | in-sensor computing | object recognition | organic–inorganic hybrid perovskites

ABSTRACT

Machine vision systems face significant challenges in accurately extracting critical features from dim objects under complex scenarios. Here, we demonstrate a ferroelectric-configured weight-reconfigurable photovoltaic device array for in-sensor dynamic computing, enabling robust recognition of dim objects. A series of 2D perovskite ferroelectric nanoplates with controllable size, high crystallinity, and excellent yield are directly synthesized. Reconfigurable and nonvolatile photovoltaics in a graphene/ferroelectric/graphene heterostructure are modulated through switchable ferroelectric polarization. Leveraging the ferroelectric-configured photoresponsivity, a convolution kernel optoelectronic sensor array with dynamic correlation of adjacent units is designed for in-sensor dynamic computing. Compared with traditional static optoelectronic convolution processing, our approach selectively amplifies subtle differences of local image pixels, enabling effective edge feature extraction even in low-contrast scenes. Integrated with a convolutional neural network, the system significantly enhances the robustness and accuracy of dim object detection, offering a promising platform for advanced machine vision applications.

1 | Introduction

Machine vision has emerged as a transformative technology that enables artificial systems to perceive and interpret the physical world. By mimicking the human visual system, it captures environmental information through sensors and leverages advanced algorithms to process, analyze, and comprehend data, facilitating efficient perception and intelligent decision-making [1, 2]. By integrating sensing, memory, and computing functionalities, in situ data processing can be achieved, eliminating redundant data migration. This enables an in-memory computing paradigm with image sensing capabilities to realize in-sensor computing [3–6].

Under complex environmental conditions, accurate extraction and interpretation of critical features from dim objects, such as varying brightness and contrast, remains a challenge. Traditional optoelectronic convolution processing, where individual units operate independently, fails to capture edge features of dim objects. To address this issue, intelligent machine vision will be an effective strategy by establishing dynamic correlations among optoelectronic units, enabling the extraction of spatial information of object features. To generate dynamic correlation between units in response to light stimuli, new optoelectronic materials are required. Common memristive materials such as HfO_x, TaO_x, and ferroelectric materials like $Hf_{0.5}Zr_{0.5}O_2$ and AlScN, despite their non-volatile characteristics, are not well-suited for high-performance photodetection [7–11]. Meanwhile, high-performance photodetectors primarily emphasize sensitive and ultrafast image sensing capabilities [12, 13]. Thus, combining the superior photosensitivity of detection materials with the non-volatile properties of ferroelectric materials presents a promising approach for implementing in-sensor computing.

The bulk photovoltaic effect (BPVE) driven by spontaneous polarization in ferroelectric materials offers notable advantages for in-sensor computing [14–16]. The ferroelectric field enables reconfigurable modulation of photoresponsivity and weight memorization [17–19]. 2D hybrid perovskite ferroelectric materials, emerging members of the ferroelectric family, have shown remarkable ferroelectric and optoelectronic properties, making them promising candidates for advanced applications [20–22]. Current synthesis methods typically employ temperature cooling crystallization, evaporative crystallization, and anti-solvent diffusion crystallization [23–28]. However, these approaches are limited by production efficiency (preparation times spanning from days to months), reagent consumption, and controllability over crystal dimensions (both thickness and planar dimensions). Therefore, the preparation of nanoscale 2D perovskite ferroelectrics with controlled uniformity notably remains a major obstacle.

In this work, we directly synthesized a series of 2D perovskite ferroelectric nanoplates using a solution-air interface floating method, including $EA_4Pb_3Br_{10}$ (EPB), $(BA)_2(EA)_2Pb_3Br_{10}$ (BEPB), and $(EA)_2(MA)_2Pb_3Br_{10}$ (EMPB). The nanoplates exhibit controllable size, good crystallinity, high yield, and excellent reproducibility. Piezoelectric response and symmetry-breaking characterizations confirmed intrinsic ferroelectricity in nanoscale thin sheets. Owing to the intrinsic photosensitivity and switchable built-in electric field, perovskite ferroelectrics enable reconfigurable and nonvolatile photovoltaics in a graphene/ferroelectric/graphene heterostructure. Leveraging the reconfigurable photoresponsivity characteristics, we developed a convolution kernel optoelectronic sensor array with dynamic correlation of adjacent units for in-sensor dynamic computing. This approach selectively amplifies subtle differences of adjacent pixels, allowing edge feature extraction from low-contrast images. When combined with a convolutional neural network (CNN), this system demonstrates robust recognition of dim traffic signs, which is challenging for conventional static optoelectronic convolution processing.

2 | Results and Discussion

2.1 | Preparation and Characterization of Perovskite Ferroelectric Nanoplates

The controllable synthesis of nano-sized 2D perovskite ferroelectrics in large quantities remains challenging. The solution-air interface floating growth method emerges as a promising approach, enabling the preparation of high-quality single-crystal nanoplates with high production efficiency and cost-effectiveness [12, 29]. As illustrated in Figure S1, single-crystalline perovskite ferroelectric nanoplates were prepared via the solution-air interface floating growth method. The process involves freestanding self-assembly at the liquid surface, followed by in-plane crystallization and layer-by-layer out-of-plane crystal growth, yielding large-area, thin, and uniform sheets (Figure S2). The formation of floating nanoplates occurs rapidly, producing morphologies with lateral dimensions of several tens of micrometers and thicknesses ranging from nanometers to hundreds of nanometers. This versatile approach enables the synthesis of various pure-phase perovskite ferroelectric nanoplates through precise control of precursor solution stoichiometry.

Figure 1a depicts the crystal structure of $EA_4Pb_3Br_{10}$ (EPB). This compound exhibits corner-sharing $[PbBr_6]^{4-}$ octahedra forming an inorganic framework, which are separated by bilayers of antiparallel organic EA^+ cations. The structure represents a classic 2D Ruddlesden-Popper (RP) perovskite. The alternating arrangement of trilayered inorganic frameworks and bilayered organic cations creates a quantum-confined structure, with organic layers serving as barriers and inorganic frameworks as quantum wells. The perovskite crystallizes in the polar space group C2cb at room temperature, featuring a highly distorted $[PbBr_6]^{4-}$ inorganic framework [30, 31].

Figure 1b shows an optical micrograph of the EPB nanoplates transferred onto a polydimethylsiloxane (PDMS) substrate. These nanoplates are mainly in rectangular shape with lateral dimensions of tens of micrometers, which are controlled by growth duration. Bright/dark field examination confirms uniform morphology, well-defined edges, and is free from contaminants (Figure 1c). Scanning electron microscopy (SEM) of individual nanoplate demonstrate flake-like morphology with sharp edges and smooth surface devoid of grain boundaries and pinholes (Figure 1d). Energy-dispersive X-ray spectroscopy (EDS) mapping confirms the uniform distribution of bromine (Br), lead (Pb), carbon (C), and nitrogen (N) elements throughout the nanoplate (Figure 1e). Meanwhile, the EDS spectrum provides a semi-quantitative analysis of the relative elemental content in the material (Figure S3).

High-resolution transmission electron microscopy (HRTEM) and selected-area electron diffraction (SAED) provided detailed insights into the microstructure and crystallinity, as shown in Figure 1f,g. HRTEM image of a transferred nanoplate shows continuous lattice fringes with an interplanar spacing of 0.33 nm, corresponding to the (0140) plane of EPB crystal structure. The SAED pattern exhibits well-defined diffraction spots in a regular rectangular array, confirming single-crystalline nature and pseudo-cubic crystal symmetry [32]. X-ray diffraction (XRD) analysis shows sharp, periodic diffraction peaks corresponding to (0h0) planes (Figure S4). No characteristic peaks from impurities or precursors were detected, indicating high phase purity of the product. Regarding the chemical states and bonding environment, X-ray photoelectron spectroscopy (XPS) was carried out (Figure 1h). A full XPS survey spectrum is provided in Figure S5, with all major peaks (C, O, N, Pb, and Br) identified and labeled. A brief note is included to attribute the O—C=O and C—O species in C 1s, and O 1s signals to adventitious surface contamination, which forms only a thin overlayer and does not affect the chemical-state analysis or conclusions [33]. In contrast, the Br 3d, Pb 4f, and N 1s core levels originating from the EPB lattice remain well defined and show no indications of degradation. In order to calibrate the peak position of C 1s, ultraviolet photoemission spectroscopy (UPS) was performed with the UV energy of 21.2 eV (Figure S6). According to the results, the work function (Φ_{SA}) of $EA_4Pb_3Br_{10}$ is approximately 4.42 eV. Using the relationship $E_B = 289.58 - \Phi_{SA}$, the corrected C 1s binding energy position is 285.16 eV [34, 35]. The N 1s spectrum shows a single peak, attributable to the amine group ($—NH^{3+}$) of the EA^+ cation, with no evidence of deprotonated species,

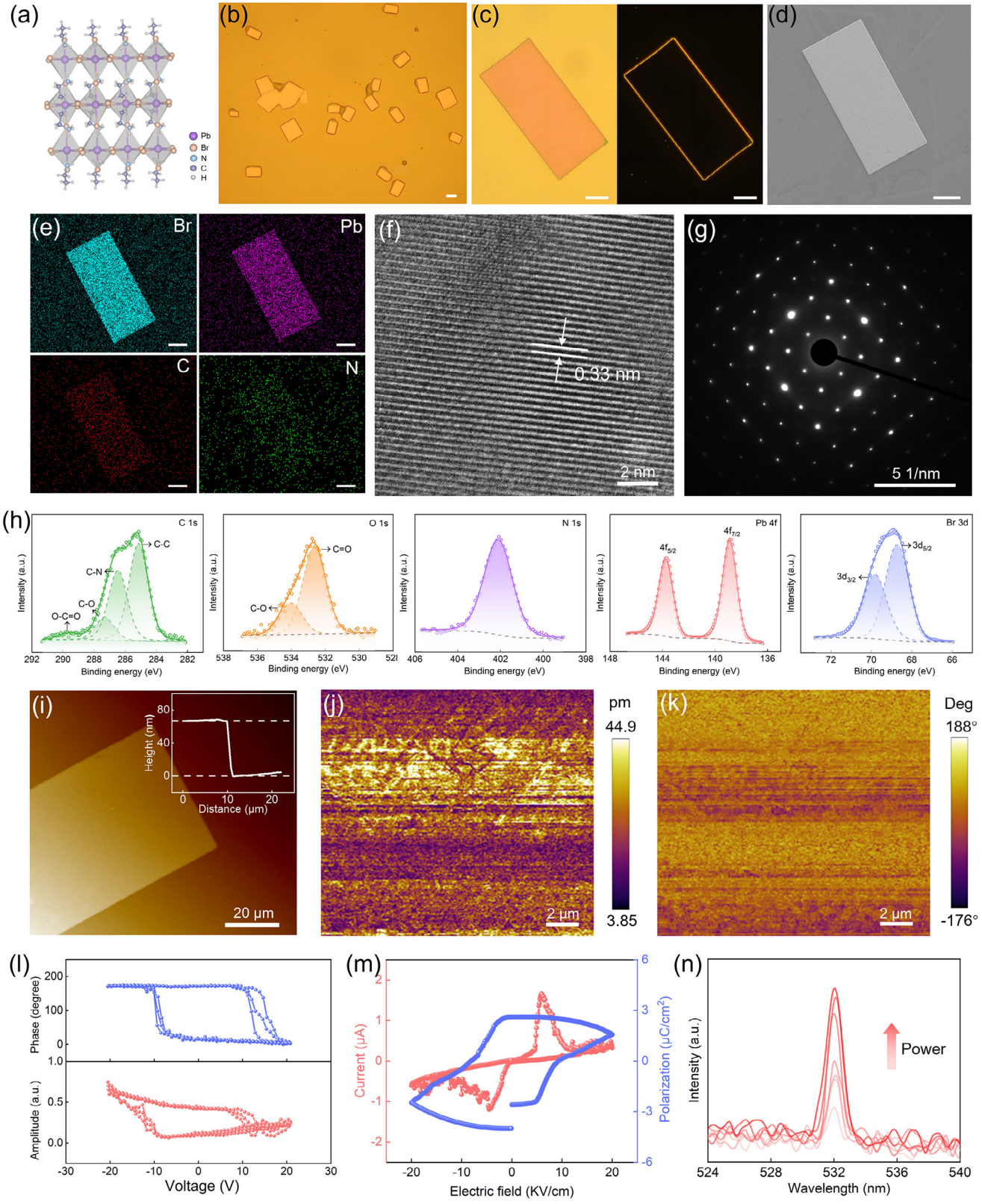

FIGURE 1 | Preparation and characterization of 2D perovskite ferroelectric nanoplates. (a) Crystal structure of EPB. (b,c) Optical image of EPB nanoplates. (d) Top-view SEM image and (e) EDS mapping of a single nanoplate. Scale bar, 20 μm. (f) HRTEM image and (g) the corresponding SAED patterns of EPB nanoplates. (h) High resolution XPS spectra of C 1s, O 1s, N 1s, Pb 4f, and Br 3d core levels. (i) AFM image of EPB nanoplate with a thickness of 67 nm. (j) Vertical PFM amplitude and (k) phase images of EPB nanoplate. (l) The phase and amplitude signals for a selected point, showing the local PFM hysteresis loops. (m) Polarization versus electric-field signals measured with a metal-semiconductor-metal structure. (n) SHG spectra of EPB nanoplates with different powers under an excitation wavelength of 1064 nm.

confirming chemical integrity and phase purity. Additionally, high-resolution XPS spectra present characteristic Br 3d and Pb 4f core-level peaks, respectively [36, 37]. The same methodology was successfully applied to batch-produce $(BA)_2(EA)_2Pb_3Br_{10}$ (BEPB) and $(EA)_2(MA)_2Pb_3Br_{10}$ (EMPB) nanoplates through systematic variation of precursor stoichiometry. Meanwhile, the same approaches were employed to conduct a thorough analysis of the as-prepared nanoplates. Comprehensive characterization using optical microscopy, SEM, EDS, HRTEM, SAED, and XRD confirmed high crystalline quality, yield, and reproducibility across all samples, establishing a robust foundation for device fabrication. Figures S7–S9 provide characterization data.

In 2D perovskite ferroelectrics, ferroelectricity typically originates from several mechanisms, including hydrogen bond distance, distortion or metal ion displacement in the octahedron, and permanent dipole molecules along a polar axis [38]. At room temperature, EPB nanoplates crystallize in a ferroelectric phase with a polar space group C2cb. For the discussion on the Curie temperature of the materials, please refer to Figure S10. The EA^+ cations maintain a specific orientation, stabilized by robust N—H···Br hydrogen bonds, while the inorganic $[PbBr_6]^{4-}$ octahedra exhibit distorted geometry [39]. This structural arrangement results in the displacement of negative charge centers in the $[PbBr_6]^{4-}$ octahedron from their ideal symmetric positions, coupled with the tilting of positive charge centers in the organic components, collectively generating a nonzero spontaneous polarization in EPB [23, 31].

To validate the ferroelectric properties, we transferred a randomly selected as-prepared nanoplate onto a gold-film-coated substrate. Piezoresponse force microscopy (PFM) was employed to investigate the ferroelectric behavior of a nanoplate with a thickness of approximately 67 nm (Figure 1i). Prior to the formal measurements, PFM was performed by sweeping the AC frequency to track the resonance frequency (Figure S11). The results show a typical frequency dependence of the PFM amplitude. Nanoscale amplitude and phase images were acquired by PFM and exhibited distinct contrast (Figure 1j,k). The phase image revealed color variations and domain walls, corresponding to different out-of-plane polarization orientations. The amplitude image displayed variations, indicating a localized electromechanical response. To directly visualize ferroelectric domain switching, we performed polarization-switching experiments by applying a local electric field. The phase and amplitude images show clear contrast, confirming the reversal of domain polarization (Figure S12). Switching spectroscopy PFM (SS-PFM) measurements were conducted at selected points to investigate polarization switching behavior (Figure 1l). A typical phase hysteresis loop and amplitude butterfly loop were observed, confirming reversible electric-field-driven polarization switching. A complete 180° polarization switching was carried out under applied tip bias voltages ranging from −20 to +20 V, demonstrating robust ferroelectricity in EPB. The asymmetry of the amplitude-voltage loop observed in the SS-PFM measurements can primarily be attributed to the presence of a built-in electric field and interfacial effects. To quantify the remnant polarization (P_r), polarization-electric field (P-E) hysteresis measurements were conducted using a metal-semiconductor-metal structure (Figure 1m). The typical P-E loop further validates ferroelectricity in EPB nanoplates. Additionally, second harmonic generation (SHG) spectroscopy, a sensitive and non-invasive technique for detecting symmetry breaking, was employed (Figure 1n). Under 1064 nm laser excitation, a strong SHG signal was detected at 532 nm, exactly half the excitation wavelength, providing further evidence of the non-centrosymmetric structure of EPB and supporting its intrinsic ferroelectric nature. Similar ferroelectric characteristics were observed in BEPB and EMPB nanoplates through PFM and SS-PFM characterization, as demonstrated in Figures S13 and S14.

2.2 | Reconfigurable Photovoltaics in Perovskite Ferroelectrics

Unlike gate-voltage modulation that requires continuous bias, the polarization-driven mechanism enables non-volatile operation, thereby eliminating static power consumption after programming and simplifying hardware implementation. Figure 2a illustrates the device architecture with a sandwich-like configuration comprising a graphene bottom electrode, a ferroelectric active layer, and a graphene top electrode in vertical alignment (Figure S15). Multilayer graphene was selected as the electrode material owing to two principal advantages: its high optical transmittance permits direct illumination and measurement of photogenerated carriers, while avoiding the Schottky barrier typically associated with metal-semiconductor contacts. The devices were fabricated using mechanical exfoliation followed by the dry-transfer technique to assemble the vertical graphene/nanoplate/graphene heterostructure. Figure 2b displays an optical micrograph of the active region. The top and bottom graphene electrodes, with thicknesses of 8 and 14 nm, along with their vertically overlapping area, are outlined by purple dashed lines (Figure 2c). A 97-nm-thick nanoplate is situated between both electrodes, forming a vertical conduction channel. This architecture facilitates efficient collection and transport of photogenerated carriers from the graphene electrodes to the external circuit.

UV–vis absorption spectroscopy was employed to characterize optical properties at room temperature. As shown in Figure 2d, a strong absorption edge is observed at approximately 445 nm, which is a characteristic absorption feature of EPB. The optical band gap was extracted using the Tauc plot method. For direct bandgap semiconductors, the relationship follows $(\alpha h\nu)^2 = A(h\nu - E_g)$, where α represents the absorption coefficient, and $h\nu$ denotes the photon energy. The calculated band gap of 2.78 eV indicates EPB's potential for short-wavelength detection applications. Using the same characterization method, we calculated that the band gaps of BEPB and EMPB are 2.92 and 2.43 eV, respectively (Figure S16). Figure 2e shows the photocurrent response to incident light power density under zero bias at 400 nm wavelength. The device shows systematic power-dependent behaviors, with photocurrent increasing monotonically as illumination intensities rise from 20 to 2000 μW cm^{-2}, demonstrating robust operation under varying lighting conditions. Furthermore, we analyzed the dynamic photoresponse characteristics, and the rise and fall times were determined to be approximately 340 and 450 ms, respectively (Figure S17). The influence of active layer thickness on self-powered performance was systematically investigated. As the nanoplate thickness increases from 25.2 to 231.7 nm, the short-circuit current (I_{sc}) exhibits a negative correlation with the thickness, while the open-circuit voltage (V_{oc}) shows an increasing trend from 0.085 to 0.246 V and reaches

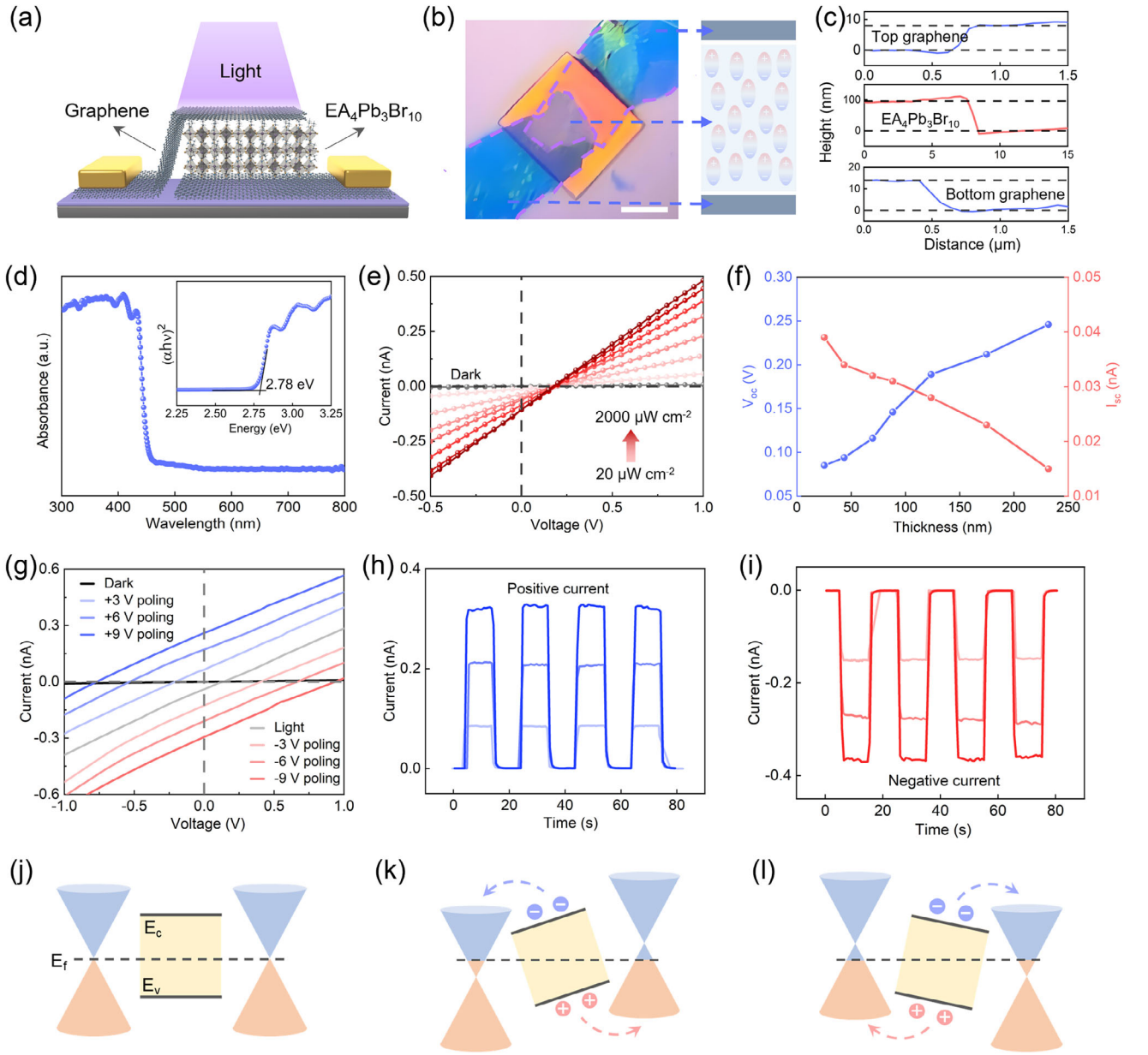

FIGURE 2 | Reconfigurable ferroelectric photovoltaics in graphene/EPB/graphene devices. (a) Schematic diagram and (b) optical image of graphene/EPB nanoplate/graphene sandwich structure. Scale bar, 20 μm. (c) Thickness of graphene and EPB layers. (d) Absorbance spectrum and corresponding Tauc plot of EPB nanoplates. (e) *I–V* curves of devices under different incident light power densities. (f) Open-circuit voltage and short-circuit current versus the thickness of nanoplates. (g) *I–V* curves of positive and negative photovoltaic behavior under different poling voltages with pulse width of 0.1 s. (h) Positive and (i) negative photoresponse in different polarization states under light power density of 1000 μW cm^{-2}. (j–l). Under illumination, energy band diagrams of graphene/nanoplate/graphene in different polarization states, demonstrating the influence of ferroelectric field on the movement of photogenerated carriers.

its maximum response at 231.7 nm thickness (Figure 2f; Figure S18). Within a certain thickness range, a thicker ferroelectric layer can sustain a larger polarization-induced internal electric field, reduce recombination loss, and enhance charge-separation efficiency-all of which contribute to an increased built-in potential and, consequently, a higher V_{oc}. Such thickness-dependent enhancement of V_{oc} is consistent with previous observations in $BiFeO_3$ and other ferroelectric photoferroelectric systems [40]. An optimal thickness range of 90–130 nm was identified for balancing device performance in ferroelectric photovoltaic applications.

The EPB nanoplates demonstrate efficient light responsivity, while their intrinsic ferroelectric polarization enables reconfigurable photovoltaic behaviors. Under 400 nm light illumination, the graphene/EPB/graphene device exhibits clear reconfigurable photovoltaic characteristics, as shown in Figure 2g and Figure S19. Polarization dependence of the photocurrent in the devices reveals seven distinct states under positive and negative poling voltages. As shown in Figure 2h,i, the photocurrent maintains comparable magnitudes under opposite polarization directions. Multiple discrete levels of both positive and negative photocurrent were observed, showing non-overlapping, step-like

transitions that confirm stable and multilevel tunability of the photoresponse via ferroelectric polarization. This reconfigurable ferroelectric photovoltaic effect was further verified in BEPB and EMPB-based devices (Figure S20). Therefore, various 2D perovskite ferroelectrics can be selectively employed to meet specific application requirements.

Figure 2j–l depicts the switchable band alignment in the heterostructure, revealing the mechanism of polarization-modulated photovoltaic behaviors. The ferroelectric polarization generates a built-in electric field that modulates energy barriers asymmetrically. Under upward polarization, the resulting built-in electric field shifts the Fermi level of bottom graphene downward, increasing the barrier height, while simultaneously elevates that of the top graphene, reducing its barrier height [19]. Thereby, this scenario promotes photogenerated carrier separation and transport. In contrast, reversing the polarization direction inverts the built-in electric field. The photocurrent magnitude is directly governed by the strength of built-in electric field, which is determined by the ferroelectric polarization state.

2.3 | Ferroelectric-Configured Photoresponsivity of Graphene/EPB/Graphene Devices

Multiple stable states are essential for achieving high computational accuracy in in-sensor image processing. The switchable ferroelectric polarization of EPB allows linear modulation of both enhancement and suppression of photoresponsivity. As illustrated in Figure 3a, continuous pulse modulation was achieved using voltage pulses ranging from −16 to +16 V with 2 V interval, inducing the upward or downward polarization states corresponding to different strengths and directions of the built-in electric field. Distinct multi-level responsivities were set under various poling voltages, comprising eight positive and eight negative states. The responsivity distribution histogram of a single device after 10 cycles shows well-separated states, confirming good reproducibility and ferroelectric tunability (Figure 3b). Long-term stability was evaluated through retention measurement over one hour, which demonstrates excellent durability of both positive and negative states, attributable to the nonvolatile character of ferroelectric polarization (Figure 3c; Figure S21). Reducing performance variations across device batches is beneficial for improving the accuracy and efficiency of image processing. To assess device-to-device uniformity, we characterized the photoresponsivity of 20 individual devices. The photoresponsivity exhibited fluctuations within a small range for each polarization state, indicating minimal differentiation and high uniformity (Figures S22 and S23). The average responsivity exhibits a well-defined linear dependence on applied voltage pulses across 16 distinct polarization states (Figure 3d). Figure 3e presents the photocurrent versus power density curves of the EPB-based devices under six distinct polarization states. The power density-photocurrent relationships were fitted using the formula $I_{ph} \propto P^{\alpha}$, yielding α values of 0.81, 0.84, 0.82, 0.83, 0.85, and 0.83, which confirms consistent sublinear dependence at all polarization states.

By applying a series of tailored voltage pulses, multiple intermediate responsivity states can be achieved between fully upward and downward polarization (Figure 3f,g). The responsivity varies linearly from −140 to 140 mA W^{-1}, enabling reversible and stable modulation of photoresponsivity. These multi-level states exhibit nonvolatile and bidirectional switching characteristics, analogous to long-term potentiation (LTP) and long-term depression (LTD) processes. The device demonstrates 30 distinguishable states, comparable to synaptic weights in artificial neural networks. The LTP and LTD processes exhibit exceptionally low nonlinearity factors of 0.17 and −0.32, respectively (Figure 3h), outperforming most reported synaptic devices (Table S1). The description of fitting process is provided in Note S1. Figure 3g further demonstrates high linearity ($R > 0.99$) and minimal variation over multiple LTP/LTD cycles. The ferroelectricity-modulated graphene/EPB/graphene devices provide a stable and efficient platform for neural network training of intelligent machine vision.

2.4 | Dynamic Brightness Adaptation and In-Sensor Convolution Kernel Processing

The switching of polarization states enables effective photosensitivity modulation of devices. Under dim light illumination, scotopic adaptation is achieved by enhancing the built-in electric field, mimicking rod cell behavior in the human retina. Conversely, under bright light illumination, photopic adaptation is realized by reducing the built-in electric field, analogous to cone cell function (Figure 4a) [41]. This self-adapting modulation allows accurate identification of both overexposed and underexposed images. As shown in Figure 4b and Figure S24, the optical adaptation capability was evaluated via a 3×3 pixel array under varying illumination. Initially in a non-polarized state, a "T"-shaped optical pattern was projected onto the device array with an incident power density of 500 μW cm^{-2}, and the pattern appeared indistinct due to low contrast. After applying negative voltage pulses to strengthen the built-in electric field, enhanced device photosensitivity enabled clear visualization of the photosensitive pixels. When the array was subsequently exposed to a high-power density light (2000 μW cm^{-2}), the pixels exhibited oversaturation and details loss due to excessive sensitivity. This issue was mitigated by applying opposite voltage pulses to weaken the built-in electric field and reduce photosensitivity, thereby preserving "T" pattern features under intense illumination. Similar functionality was also achieved under positive polarization conditions (Figure S25).

Leveraging the linear modulation of photoresponsivity, various convolution kernels can be constructed for image processing by individually adjusting the weights of each sub-pixel [42, 43]. Figure 4c displays the original gray image used for edge detection. Figure S26 and Figure 4d present two Sobel operators and their corresponding responsivity configurations, respectively. These convolution kernels were used to extract image edge information along X- and Y-axis directions. A feature map of image edges was obtained via combining the X and Y-axis direction results. The experimental results using ferroelectric-configured convolution kernels align well with software simulations (Figure 4e,f). Furthermore, the device array demonstrates potential for image sharpening applications, as illustrated in Figure S27. Integration of the proposed ferroelectric-configured convolution kernels with convolutional neural network (CNN) holds promise for breakthroughs in the field of image recognition.

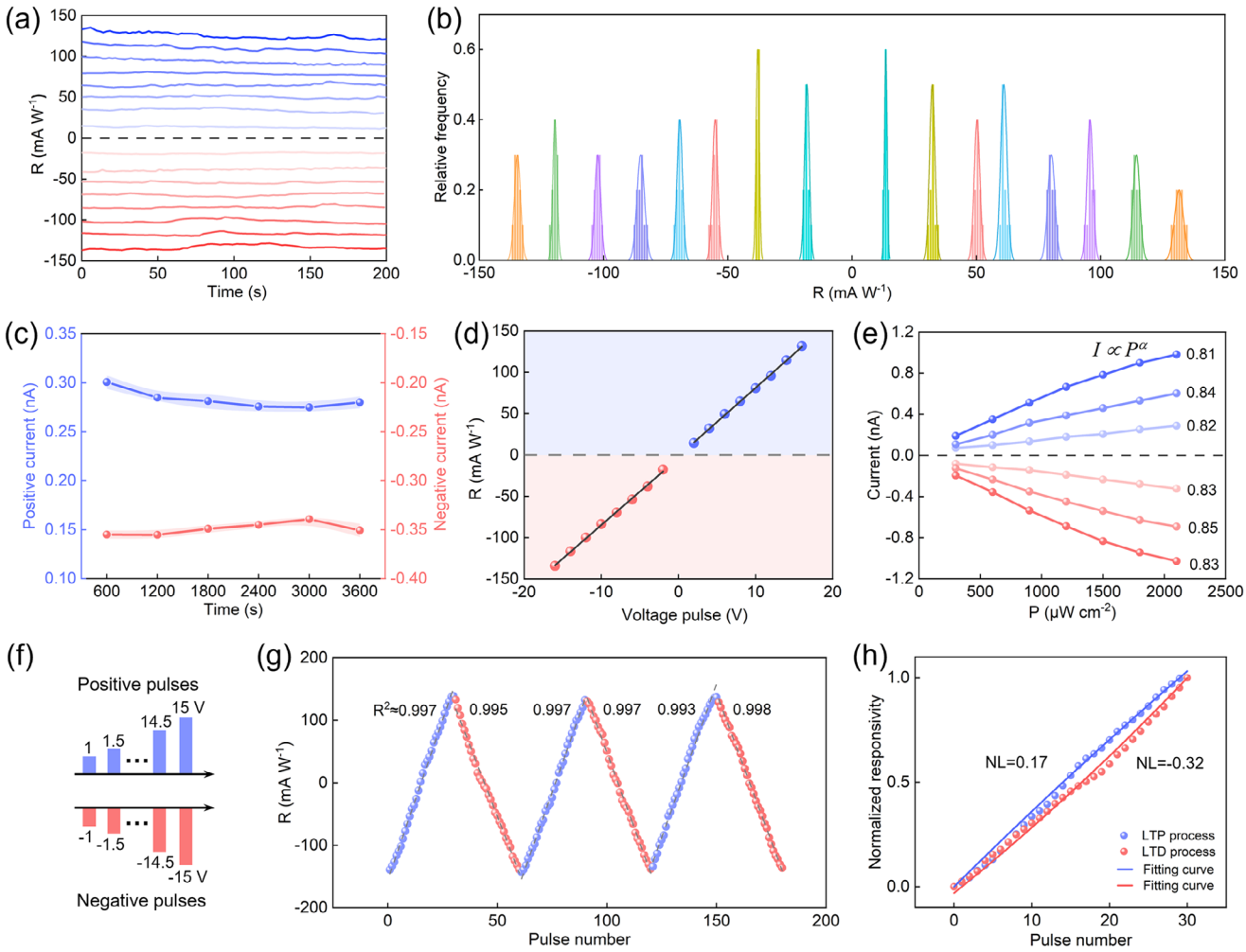

FIGURE 3 | Ferroelectric-configured photoresponsivity of graphene/EPB/graphene devices. (a) Responsivities under eight positive and eight negative polarization states under 400 nm light illumination (poling voltages ranging from −16 to 16 V with 2 V interval). (b) Well-separated responsivity distribution histogram of a device after 10 cycles. (c) Long-term stability of positive and negative states. (d) Average responsivity of 20 devices at 16 distinct polarization states. (e) Photocurrent versus power density under different polarization states. (f) A series of voltage pulses with pulse width of 0.1 s used for state update. (g) Three-cycle photoresponsivity LTP and LTD weight update modulated by the voltage pulses. (h) Nonlinear fitting of LTP and LTD processes.

2.5 | In-Sensor Dynamic Computing for Dim Object Recognition

Developing an intelligent machine vision system is fundamental for perceiving the physical world. Accurate extraction and interpretation of critical features from dim objects under various conditions (e.g., changes in brightness and contrast) demands enhanced capabilities in data preprocessing and intelligent recognition. Conventional static optoelectronic convolution processing, where individual units operate independently, fails to capture spatial correlations in object features, thus limiting its ability to recognize dim objects. To overcome this limitation, we implement in-sensor dynamic computing by establishing dynamic correlations among optoelectronic units within the array, enabling the extraction of object features from spatially correlated difference signals (Figure 5a) [4]. As shown in Figure 5b, traffic signs exhibit significantly reduced contrast under dim light conditions. While traditional methods struggle to extract edge features from such low-contrast images, in-sensor dynamic computing remains effective and accurately retrieves edge information. Comparative results for edge feature extraction from additional traffic signs are provided in Figure S28. Figure 5c illustrates the in-sensor dynamic computing process employing decision and dynamic kernels. Two decision kernels are edge detection kernels along the X- and Y-directions, which determine the configuration of active unit in the dynamic kernel. The array units in the dynamic kernel are classified into two types: active unit (purple) and static unit (orange). Static units respond solely to local pixel signals, whereas active units, positioned at the kernel center, correlate the output with both local and surrounding pixels. It selectively amplifies the subtle differences between local and peripheral regions, thereby facilitating effective edge feature extraction even in low-contrast scenes. An algorithm flowchart for dim object edge detection is provided in Figure S29.

The integration of ferroelectric-configured convolution kernels with a CNN enables effective dim object recognition. To further address the inherent performance variations among individual

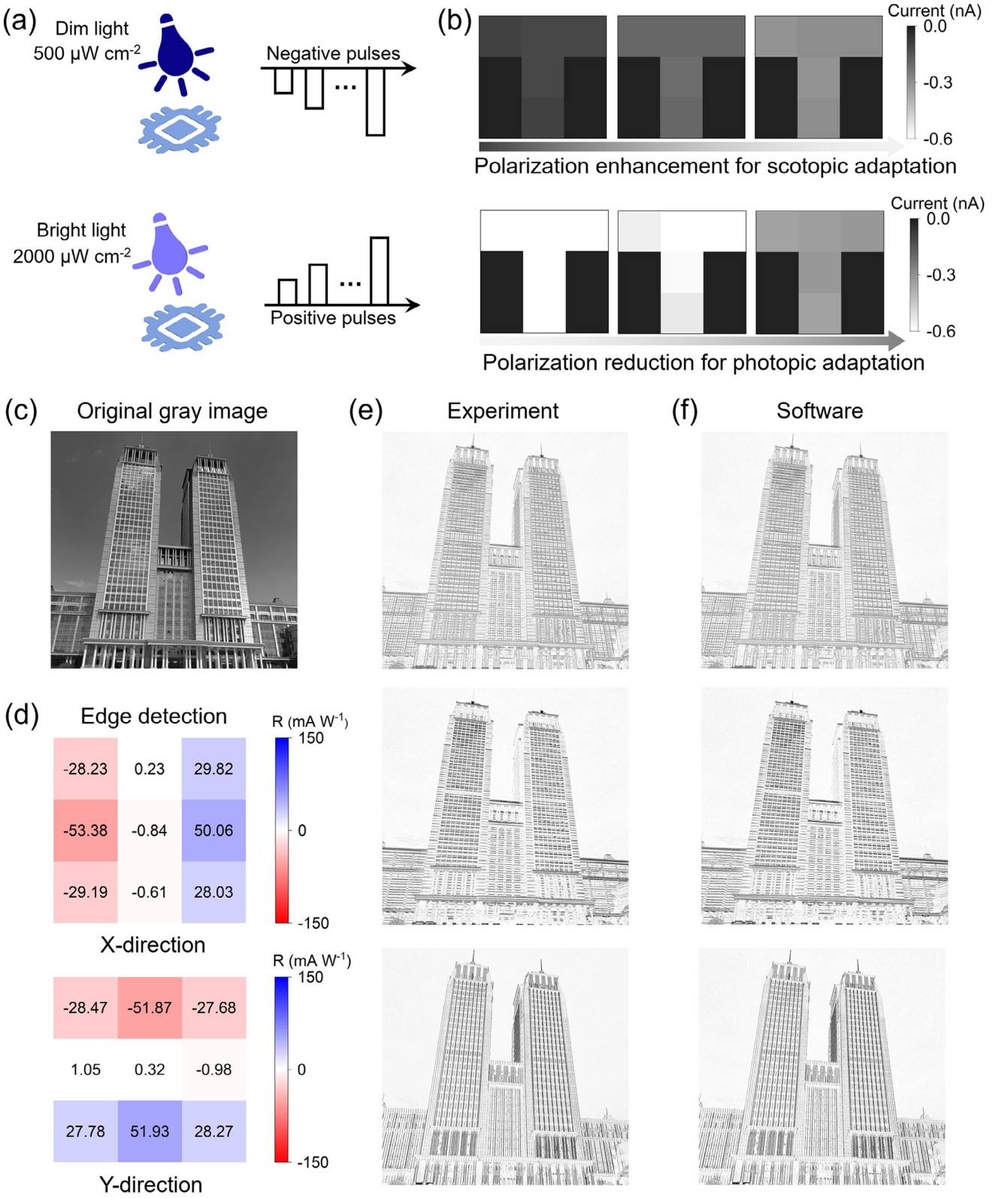

FIGURE 4 | Dynamic brightness adaptation and edge detection. (a) Schematic of scotopic and photopic adaptation under dim and bright illumination. (b) Scotopic and photopic adaptation processes carried out on a 3 × 3 pixel array. (c) Original gray image for edge detection convolutional processing. (d) Actual responsivity configurations in two convolution kernels to perform edge detection in X and Y directions. (e) Experiment edge detection results based on convolution kernels in (d) (Top: Combined feature map, Middle: X-direction, Bottom: Y-direction). (f) Software edge detection results based on Sobel operators provided in Figure S26.

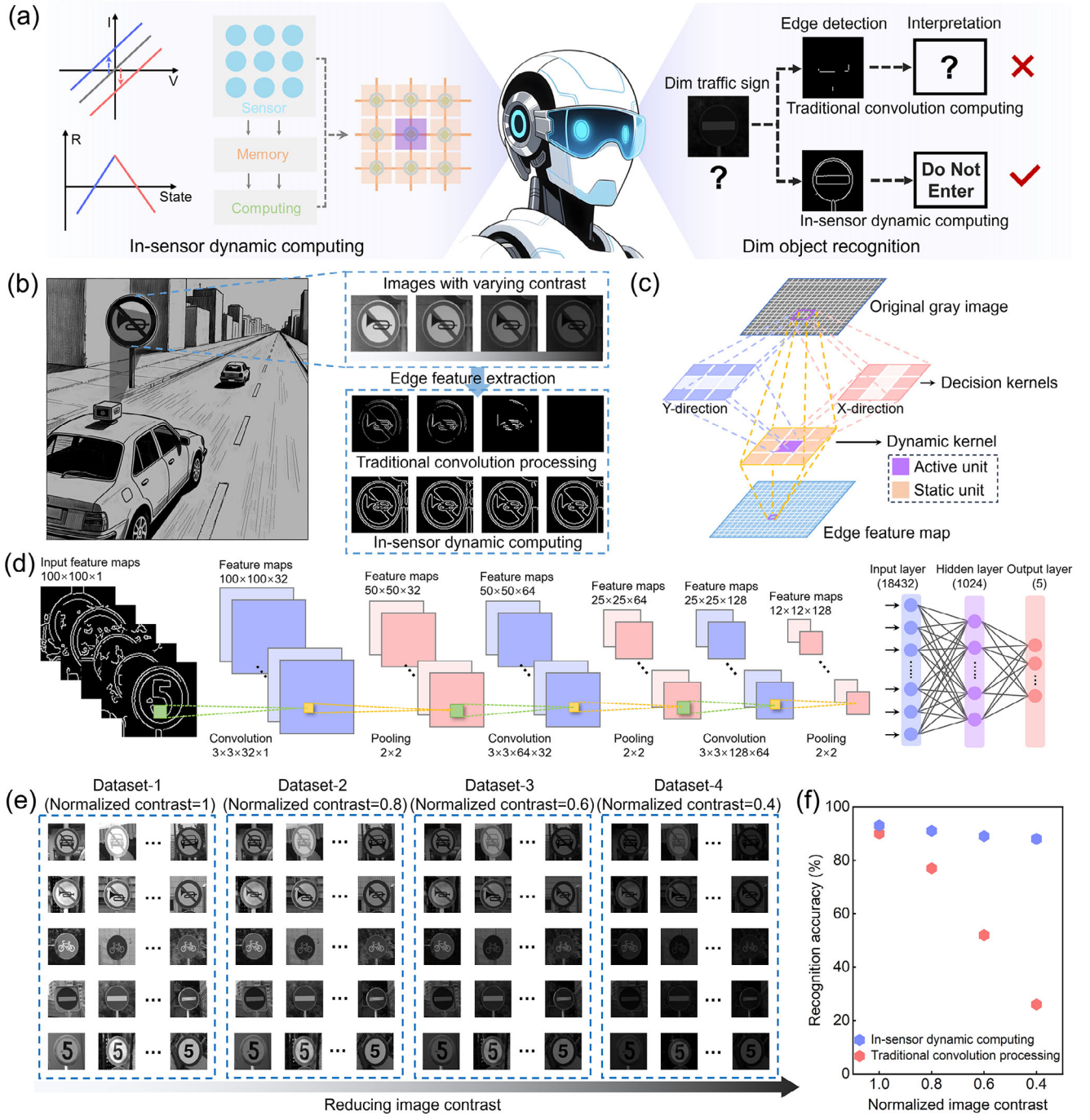

FIGURE 5 | Ferroelectric-configured in-sensor dynamic computing for dim object recognition. (a) Left: In-sensor dynamic computing architecture integrating image sensing, weight memorization, and computing functions. Right: In-sensor dynamic computing for edge detection and dim object recognition. (b) Edge feature extraction of images with varying contrast. (c) Schematic of edge feature extraction based on the dynamic convolution kernels. (d) Feature maps recognition based on the 8-layer CNN architecture. e) Four extended datasets based on CTS dataset. (f) Recognition accuracy of the four datasets after 150 training epochs.

array elements, a straightforward yet effective data-processing strategy was implemented. Central to this approach is the introduction of "reference devices" that serve as a standardized performance benchmark. After uniformly characterizing all array units, a simple mathematical normalization procedure is applied. This step does not alter the physical properties of the devices but rather calibrates the measured data to a common reference condition. Consequently, the comparison of performance across the array genuinely reflects the relative capabilities of each unit under equivalent idealized conditions. Figure 5d shows the employed CNN architecture, which comprises an 8-layer network with 18,432 input neurons, 1,024 hidden neurons, and 5 output neurons, specifically designed for feature map recognition. Experiments were conducted using an adapted Chinese traffic sign (CTS) dataset with 5 object categories. Four datasets with different normalized contrast were utilized, each consisting of

1,000 training and 200 testing images (Figure 5e). We compared the recognition accuracy of traffic signs between in-sensor dynamic computing and conventional optoelectronic convolution processing across these datasets. As summarized in Figure 5f, in-sensor dynamic computing achieved 88–93% recognition accuracy under 150 epochs, with accurate edge feature extraction being key to this robust performance. In contrast, the accuracy of traditional convolution processing declines as normalized contrast decreases. Recognition accuracy curves and confusion matrices for all datasets are provided in Figures S30 and S31. These results demonstrate that ferroelectric-configured in-sensor dynamic computing maintains high recognition accuracy, highlighting its potential for intelligent machine vision in low-light and complex scenarios.

3 | Conclusion

In this study, we have implemented a ferroelectric-configured weight-reconfigurable photovoltaic device array leveraging the BPVE in perovskite ferroelectrics. 2D perovskite ferroelectric nanoplates were directly synthesized via a solution-air interface floating growth method, exhibiting controlled dimensionality, high crystallinity, excellent yield, and reproducibility. Switchable ferroelectric polarization enables reconfigurable and nonvolatile photoresponsivity for in-sensor dynamic computing, which is significantly superior to conventional approaches in extracting edge features from dim objects. When integrated with a CNN, the system achieved 88–93% recognition accuracy of traffic signs with varying contrast. This work provides a promising platform for developing intelligent machine vision systems capable of operating in complex visual environments.

4 | Experimental Section

4.1 | Materials

Ethylammonium Bromide (EABr, 99.9%), Butylammonium Bromide (BABr, 99.9%), Methylamine Bromide (MABr, 99.9%) were purchased from Advanced Election Technology Co., Ltd. Lead bromide ($PbBr_2$, 99.999%) and Hydrobromic acid (HBr, 48 wt.% in H_2O) were purchased from Aladdin Scientific Corp. The graphene crystals were purchased from SixCarbon Technology Company. All chemicals were used without further treatment.

4.2 | Nanoplates Synthesis

The organic–inorganic hybrid perovskite ferroelectric nanoplates were synthesized using a solution-air interface method, as shown in Figure S1. Taking EPB as an example: EABr (0.45 g) and $PbBr_2$ (0.99 g) were dissolved in 3 mL hydrobromic acid solution. The mixture was heated under continuous stirring at 120°C until a clear yellow solution formed. Subsequently, the solution was cooled to 60°C and stored in a sealed glass vial. A small aliquot of the warm supernatant was extracted via pipette and dropped onto a hydrophobically treated glass slide. Nanoplates crystallized within seconds at the droplet surface. The nanoplates were collected using a PDMS stamp brought into contact with the droplet surface. The residual solution was removed using nitrogen gas flow. Following the same protocol, precursor solutions for BEPB and EMPB were prepared with the following compositions: For BEPB: BABr (0.15 g), EABr (0.09 g), and $PbBr_2$ (0.37 g) were dissolved in 3 mL hydrobromic acid solution. For EMPB: EABr (0.23 g), MABr (0.07 g), and $PbBr_2$ (0.44 g) were dissolved in 3 mL hydrobromic acid solution.

4.3 | Device Fabrication

Few-layer graphene was mechanically exfoliated from the bulk crystal. A dry transfer technique was implemented using a 2D transfer platform to precisely position the nanomaterials. The graphene layers and perovskite nanoplates were vertically assembled to construct a graphene/nanoplate/graphene sandwich heterostructure. Device patterning was accomplished using a transmission electron microscopy copper grid as a shadow mask, followed by thermal evaporation of Cr (5 nm)/Au (30 nm) electrodes.

4.4 | Measurement and Characterization

Optical images were captured by an optical microscope (BX51M, Olympus). X-ray diffraction (XRD) patterns were recorded by X-ray diffractometer (Bruker D8). PL spectra were measured by Renishaw in Via-Qontor Raman microscope equipped with 325 nm laser. Absorption spectra were recorded via an ultraviolet-visible spectrophotometer (U-3900H, Hitachi). Ultraviolet photoemission spectroscopy (UPS) and X-ray photoelectron spectroscopy (XPS) were performed using a Thermo Scientific K-Alpha spectrometer equipped with a monochromatic Al Kα source ($h\nu$ = 1486.6 eV). The X-ray spot size was 400 µm, and the electron emission angle was 60°. The base pressure in the analysis chamber was maintained below 5.0×10^{-7} mbar. The samples were mounted on a conductive holder and electrically connected to the spectrometer. A low-energy electron flood gun was employed for charge neutralization. No Ar^+ sputter etching was applied. The scanning electron microscope (SEM) and energy-dispersive X-ray spectroscopy (EDS) were performed on a Zeiss Sigma 300 instrument. High-resolution transmission electron microscope (HRTEM) and selected-area electron diffraction (SAED) were carried out on a FEI Talos F200X G2 instrument. The phase transition temperature was measured using a differential scanning calorimetry (Q2000, TA). Atomic force microscopy (AFM) measurements were performed on a Bruker Dimension Icon. Local piezoelectric response and polarization direction at the nanometer scale were characterized by a piezoresponse force microscopy (Cypher S, Oxford Instruments; AFM Pro, Truth Instruments). Second harmonic generation (SHG) measurement was carried out to analyze the non-centrosymmetric characteristics using a laser source with a wavelength of 1064 nm. The electrical and optoelectronic measurements were carried out using a Keithley 4200-S semiconductor test system connected to a vacuum probe station. A 75 W xenon lamp with continuously tunable wavelength was used as light sources. The power density was measured via an Ophir Photonics NOVA II optical power meter. All tests were performed at room temperature.

4.5 | Neuromorphic Computing for Image Recognition

The Chinese traffic sign (CTS) database is an open database and was downloaded from the website (https://nlpr.ia.ac.cn/pal/trafficdata/index.html). The processed feature maps were flattened and input into a convolutional neural network (CNN). The CNN architecture consists of input layer, convolution layer, pooling layer, and fully connected layer. The training process is based on experimental LTP and LTD curves, as shown in Figure 3g. The neural network was trained using back-propagation and the gradient descent algorithm, employing a learning rate of 0.001 and batch size of 32.

Acknowledgements

The work was supported by the National Natural Science Foundation of China (Grant Nos. 52425308, 62374035, and 92263106) and the China Postdoctoral Science Foundation (2023M730611). The authors acknowledge Q.Z. for his valuable contributions to the development of neural network architecture.

Conflicts of Interest

The authors declare no conflicts of interest.

Data Availability Statement

The data that support the findings of this study are available in the supplementary material of this article.

References

1. Y. Chai, "In-sensor Computing for Machine Vision," *Nature* 579 (2020): 32, https://doi.org/10.1038/d41586-020-00592-6.

2. L. Mennel, J. Symonowicz, S. Wachter, D. K. Polyushkin, A. J. Molina-Mendoza, and T. Mueller, "Ultrafast Machine Vision with 2D Material Neural Network Image Sensors," *Nature* 579 (2020): 62–66, https://doi.org/10.1038/s41586-020-2038-x.

3. Q. Ren, C. Zhu, and S. Ma, et al., "Optoelectronic Devices for In-Sensor Computing," *Advanced Materials* 37 (2025): 2407476, https://doi.org/10.1002/adma.202407476.

4. Y. Yang, C. Pan, Y. Li, et al., "In-sensor Dynamic Computing for Intelligent Machine Vision," *Nature Electronics* 7 (2024): 225–233, https://doi.org/10.1038/s41928-024-01124-0.

5. J. Liu, M. Zhang, W. Han, F. Du, L. Wu, and X. Fang, "Ferroelectric-Gated Hybrid-Layered Organic Field-Effect Transistors for Multimode Signal Processing," *Advanced Functional Materials* 35 (2025): 08765, https://doi.org/10.1002/adfm.202508765.

6. J. Liu, W. Han, E. Hong, et al., "In-Memory Sensing and Logic Processing in Negative Capacitance Phototransistors," *Advanced Functional Materials* 35 (2025): 2425350, https://doi.org/10.1002/adfm.202425350.

7. X. Duan, Z. Cao, K. Gao, et al., "Memristor-Based Neuromorphic Chips," *Advanced Materials* 36 (2024): 2310704, https://doi.org/10.1002/adma.202310704.

8. T. Jin, K. Lv, J. Chen, L. Zhang, and X. Guo, "Fully Hardware-implemented Neuromorphic Systems Using TaOx-based Memristors," *Device* 3 (2025): 100645.

9. J. Zhang, K. Xu, L. Lu, et al., "Ferroelectric/Antiferroelectric HfZrO x Artificial Synapses/Neurons for Convolutional Neural Network–Spiking Neural Network Neuromorphic Computing," *Nano Letters* 25 (2025): 13739–13747, https://doi.org/10.1021/acs.nanolett.5c02889.

10. J. Lee, R. Shenoy, A. Deo, et al., "HfZrO-based Synaptic Resistor Circuit for a Super-Turing Intelligent System," *Science Advances* 11 (2025): adr2082, https://doi.org/10.1126/sciadv.adr2082.

11. Z. Xie, K. Jiang, S. Zhang, et al., "Nonvolatile and Reconfigurable Two-terminal Electro-optic Duplex Memristor Based on III-nitride Semiconductors," *Light: Science & Applications* 13 (2024): 78, https://doi.org/10.1038/s41377-024-01422-4.

12. E. Hong, Z. Li, X. Zhang, X. Fan, and X. Fang, "Deterministic Fabrication and Quantum-Well Modulation of Phase-Pure 2D Perovskite Heterostructures for Encrypted Light Communication," *Advanced Materials* 36 (2024): 2400365, https://doi.org/10.1002/adma.202400365.

13. M. Deng, Z. Li, X. Deng, Y. Hu, and X. Fang, "Wafer-scale Heterogeneous Integration of Self-powered Lead-free Metal Halide UV Photodetectors With Ultrahigh Stability and Homogeneity," *Journal of Materials Science & Technology* 164 (2023): 150–159, https://doi.org/10.1016/j.jmst.2023.05.007.

14. Y. Li, J. Fu, X. Mao, et al., "Enhanced Bulk Photovoltaic Effect in Two-dimensional Ferroelectric CuInP2S6," *Nature Communications* 12 (2021): 5896, https://doi.org/10.1038/s41467-021-26200-3.

15. R. Nanae, S. Kitamura, Y.-R. Chang, et al., "Bulk Photovoltaic Effect in Single Ferroelectric Domain of SnS Crystal and Control of Local Polarization by Strain," *Advanced Functional Materials* 34 (2024): 2406140, https://doi.org/10.1002/adfm.202406140.

16. T. Li, J. Miao, X. Fu, et al., "Reconfigurable, Non-Volatile Neuromorphic Photovoltaics," *Nature Nanotechnology* 18 (2023): 1303–1310, https://doi.org/10.1038/s41565-023-01446-8.

17. Z. Dang, F. Guo, Z. Wang, et al., "Object Motion Detection Enabled by Reconfigurable Neuromorphic Vision Sensor Under Ferroelectric Modulation," *ACS Nano* 18 (2024): 27727–27737, https://doi.org/10.1021/acsnano.4c10231.

18. G. Wu, X. Zhang, G. Feng, et al., "Ferroelectric-defined Reconfigurable Homojunctions for In-memory Sensing and Computing," *Nature Materials* 22 (2023): 1499–1506, https://doi.org/10.1038/s41563-023-01676-0.

19. Y. Gong, R. Duan, Y. Hu, et al., "Reconfigurable and Nonvolatile Ferroelectric Bulk Photovoltaics Based on 3R-WS2 for Machine Vision," *Nature Communications* 16 (2025): 230, https://doi.org/10.1038/s41467-024-55562-7.

20. H. Hu, Z.-Y. Jing, Q. Pan, et al., "Organic–Inorganic Hybrid Perovskite for Ferroelectric Catalysis," *Advanced Materials* 36 (2024): 2413547, https://doi.org/10.1002/adma.202413547.

21. W. Zheng, X. Wang, X. Zhang, et al., "Emerging Halide Perovskite Ferroelectrics," *Advanced Materials* 35 (2023): 2205410, https://doi.org/10.1002/adma.202205410.

22. F. Du, J. Liu, W. Han, E. Hong, and X. Fang, "Low-Power Optoelectronic Hybrid Perovskite-Based Memristor for Ternary Hardware Security Monitoring," *Advanced Functional Materials* 35 (2025): 16930, https://doi.org/10.1002/adfm.202516930.

23. S. Han, Y. Ma, L. Hua, et al., "Soft Multiaxial Molecular Ferroelectric Thin Films With Self-Powered Broadband Photodetection," *Journal of the American Chemical Society* 144 (2022): 20315–20322, https://doi.org/10.1021/jacs.2c07892.

24. Y. Hu, H. Lu, S. B. Masood, et al., "A 2D Hybrid Perovskite Ferroelectric with Switchable Polarization and Photoelectric Robustness Down to Monolayer," *Nature Communications* 16 (2025): 3028, https://doi.org/10.1038/s41467-025-58164-z.

25. Z.-X. Zhang, H. Wang, H.-F. Ni, et al., "Organic-Inorganic Hybrid Ferroelectric and Antiferroelectric With Afterglow Emission," *Angewandte Chemie International Edition* 63 (2024): 202319650, https://doi.org/10.1002/anie.202319650.

26. T.-T. Sha, X.-C. Zhang, R.-J. Zhou, et al., "Organic–Inorganic Hybrid Perovskite Ferroelectric Nanosheets Synthesized by a Room-Temperature

Antisolvent Method," *Advanced Science* 11 (2024): 2400636, https://doi.org/10.1002/advs.202400636.

27. I.-H. Park, K. C. Kwon, Z. Zhu, et al., "Self-Powered Photodetector Using Two-Dimensional Ferroelectric Dion–Jacobson Hybrid Perovskites," *Journal of the American Chemical Society* 142 (2020): 18592–18598, https://doi.org/10.1021/jacs.0c08189.

28. G. M. Anilkumar, M. Bhakar, C. Taneja, et al., "Near Room Temperature Solvothermal Growth of Ferroelectric CsPbBr 3 Nanoplatelets With Ultralow Dark Current," *Advanced Materials* 36 (2024): 2403875, https://doi.org/10.1002/adma.202403875.

29. D. Pan, Y. Fu, N. Spitha, et al., "Deterministic Fabrication of Arbitrary Vertical heterostructures of two-dimensional Ruddlesden–Popper halide perovskites," *Nature Nanotechnology* 16 (2021): 159, https://doi.org/10.1038/s41565-020-00802-2.

30. K. Tao, C. Xiong, H. Yang, et al., "Anisotropic X-ray Photovoltaics in 2D Trilayered Hybrid Perovskite EA 4 Pb 3 Br 10 Single Crystals With a Low Detection Limit," *Inorganic Chemistry Frontiers* 11 (2024): 5624–5635, https://doi.org/10.1039/D4QI00934G.

31. L. Mao, Y. Wu, C. C. Stoumpos, et al., "Tunable White-Light Emission in Single-Cation-Templated Three-Layered 2D Perovskites (CH 3 CH 2 NH 3) 4 Pb 3 Br 10– x Cl x," *Journal of the American Chemical Society* 139 (2017): 11956–11963, https://doi.org/10.1021/jacs.7b06143.

32. Y. Zhang, E. Parsonnet, A. Fernandez, et al., "Ferroelectricity in a Semiconducting All-inorganic Halide Perovskite," *Science Advances* 8 (2022): abj5881, https://doi.org/10.1126/sciadv.abj5881.

33. G. Greczynski and L. Hultman, "Impact of Sample Storage Type on Adventitious Carbon and Native Oxide Growth: X-ray Photoelectron Spectroscopy Study," *Vacuum* 205 (2022): 111463.

34. G. Greczynski and L. Hultman, "Binding Energy Referencing in X-ray Photoelectron Spectroscopy," *Nature Reviews Materials* 10 (2025): 62–78, https://doi.org/10.1038/s41578-024-00743-5.

35. G. Greczynski and L. Hultman, "Reliable Determination of Chemical State in X-ray Photoelectron Spectroscopy based on Sample-work-function Referencing to Adventitious Carbon: Resolving the Myth of Apparent Constant Binding Energy of the C 1s peak," *Applied Surface Science* 451 (2018): 99–103, https://doi.org/10.1016/j.apsusc.2018.04.226.

36. W.-C. Lin, W.-C. Lo, J.-X. Li, Y.-K. Wang, J.-F. Tang, and Z.-Y. Fong, "In situ XPS Investigation of the X-ray-triggered Decomposition of Perovskites in Ultrahigh Vacuum Condition," *Npj Materials Degradation* 5 (2021): 13, https://doi.org/10.1038/s41529-021-00162-9.

37. G. Greczynski, R. T. Haasch, N. Hellgren, E. Lewin, and L. Hultman, "X-ray Photoelectron Spectroscopy of Thin Films," *Nature Reviews Methods Primers* 3 (2023): 40, https://doi.org/10.1038/s43586-023-00225-y.

38. K. Leng, R. Li, S. P. Lau, and K. P. Loh, "Ferroelectricity and Rashba Effect in 2D Organic–inorganic Hybrid Perovskites," *Trends in Chemistry* 3 (2021): P716–732, https://doi.org/10.1016/j.trechm.2021.05.003.

39. Y. Liu, D. Chen, Z. Zhang, W. Li, and J. Fan, "Emerging Low-dimensional Perovskite Photoferroelectrics: From Crystallographic Microstructure to Applications," *Nano Energy* 136 (2025): 110774, https://doi.org/10.1016/j.nanoen.2025.110774.

40. S. Y. Yang, L. W. Martin, and S. J. Byrnes, et al., "Photovoltaic Effects in BiFeO3," *Applied Physics Letters* 95 (2009): 062909, https://doi.org/10.1063/1.3204695.

41. Y. Wang, S. Gou, X. Dong, et al., "A Biologically Inspired Artificial Neuron with Intrinsic Plasticity based on Monolayer Molybdenum Disulfide," *Nature Electronics* 8 (2025): 680–688, https://doi.org/10.1038/s41928-025-01433-y.

42. J. Si, P. Zhang, C. Zhao, et al., "A Carbon-nanotube-Based Tensor Processing Unit," *Nature Electronics* 7 (2024): 684–693, https://doi.org/10.1038/s41928-024-01211-2.

43. L. Xu, J. Liu, X. Guo, et al., "Ultrasensitive Dim-light Neuromorphic Vision Sensing Via Momentum-conserved Reconfigurable Van Der Waals Heterostructure," *Nature Communications* 15 (2024): 9011, https://doi.org/10.1038/s41467-024-53268-4.

Supporting Information

Additional supporting information can be found online in the Supporting Information section.

Supporting File: adma71920-sup-0001-SuppMat.docx